Materials Science & Engineering A 664 (2016) 227–235

Contents lists available at ScienceDirect

Materials Science & Engineering A

journal homepage: www.elsevier.com/locate/msea

Hot deformation behaviour and processing map of Co-Cu-Fe-Ni-Ti eutectic high entropy alloy

Sumanta Samal *, M.R. Rahul, Ravi Sankar Kottada, Gandham Phanikumar

Department of Metallurgical and Materials Engineering, Indian Institute of Technology Madras, Chennai 600036, Tamil Nadu, India

ARTICLE INFO

Article history:
Received 29 February 2016
Received in revised form
4 April 2016
Accepted 5 April 2016
Available online 6 April 2016

Keywords:
Eutectic high entropy alloy
Flow behaviour
Processing map
Efficiency power dissipation
Gleeble®

ABSTRACT

Multicomponent $Co_{20}Cu_{20}Fe_{20}Ni_{20}Ti_{20}$ eutectic high entropy alloy (HEA), processed by vacuum arc melting cum suction casting technique was studied. The microstructure of this eutectic HEA consists bcc (β) and fcc (α_2) solid solution dendritic phases and eutectics (fcc (α_1) plus Ti_2(Ni, Co)-type Laves phase). Serrations in the flow behaviour are attributed to multi substitutional solutes in the multi-phase microstructure. Based on the detailed analysis of mechanical data together with deformed microstructural characterization, the optimum thermo-mechanical processing conditions for hot working are identified as T=930–990 °C (1203–1263 K) and strain rate range of 10^{-3} s^{-1}–10^{-1} s^{-1}.

1. Introduction

A recent review of open literature [1,2] in the last decade on the multicomponent alloys designates high entropy alloys as promising candidate materials in various potential applications due to their outstanding properties. The concept of multicomponent equiatomic or near equiatomic HEAs was first advocated by Yeh et al. [3], which has closely been followed by many research groups across the globe [4–9]. Earlier, it was anticipated that the multicomponent alloys are associated with intermetallic phases, complex microstructure and poor mechanical properties [3–5]. On the contrary, the microstructures of the HEAs are experimentally often found to be consisting of single phase solid solutions of FCC and/or BCC phases. Single phase solid solutions are hypothesized to form due to high configurational entropy associated with equiatomic mixing, which minimizes their free energy. These simple structures also show excellent thermal stability at high temperatures [10,11]. There are several effects of alloying multiple elements [1] such as high entropy, severe lattice distortion and sluggish diffusion [12,13] which enable to interfere with complex phase formation, slow down phase transformations and consequently alter properties. Nevertheless, the understanding of the physical metallurgy of multicomponent HEAs is still at its beginning stage. Several future research trends in the field of HEAs can be foreseen.

Yeh et al. [3] investigated the microstructure and properties of $CuCoNiCrAl_xFe$ alloys produced by casting and splat quenching and found that these alloys maintained their strength up to 500 °C. Senkov et al. [14] synthesized the refractory $Nb_{25}Mo_{25}Ta_{25}W_{25}$ and $V_{20}Nb_{20}Mo_{20}Ta_{20}W_{20}$ HEAs and observed the retention of strength of refractory HEAs at high temperature. The microstructural evolution [15], room temperature mechanical properties [16] and phase stability [17] of Ti-Cu-Fe-Co-Ni HEA have been reported recently in the literature. In the last few years, a lot of research work has been under progress in finding the new compositions as well as new types of multicomponent HEAs. Therefore, multicomponent eutectic high entropy alloys consisting of both solid solution phases and eutectics can be considered as potential candidates for high temperature structural applications.

Manufacturing process on novel alloys can be designed only by understanding the flow stress behaviour and the microstructure control during hot working processes [18]. And microstructure is greatly influenced by thermo-mechanical processing parameters such as temperature, strain rate and strain during deformation at elevated temperature. The hot deformation behaviour and processing maps of titanium alloys [19,20], magnesium alloys [21,22], superalloys [23–25] has been very well documented in the literature. However, there have been very limited studies on thermo-mechanical processing (TMP) of HEAs and processing maps of HEAs because of their high strength and low ductility even at elevated temperature [26,27]. Further, the fundamental understanding of the principle mechanisms for the serrations in flow behaviour, and the correlation of the deformed microstructural

* Corresponding author.
E-mail address: sumantasamal1985@gmail.com (S. Samal).

http://dx.doi.org/10.1016/j.msea.2016.04.006
0921-5093/

features with the generated deformation processing map of eutectic high entropy alloys has not been documented sufficiently in the literature.

Thus, the objective of the present investigation is to identify optimum TMP conditions to obtain defect free hot worked products. This is achieved by studying the influence of temperature and strain rate on the deformation characteristics of multicomponent equiatomic Co-Cu-Fe-Ni-Ti eutectic HEA. In the present study, the TMP of multicomponent eutectic HEA was carried out, and the deformation processing maps were developed.

2. Experimental materials and procedures

High purity commercial Co, Cu, Fe, Ni and Ti ($\geq$ 99.9%) were used as the starting materials. The multicomponent Co, Cu, Fe, Ni and Ti alloy was synthesized by arc melting under ultra high purity argon gas on water cooled copper hearth to obtain arc melted alloy button. The arc melted alloy button was subsequently suction casting into a water-cooled split Cu-mold to obtain cylindrical rod having 10 mm diameter and aspect ratio of 7:1. The phase identification of suction cast cylinders (ϕ=10 mm) was examined by X-ray diffraction (XRD) (Panalytical X-pert pro instrument) with Cu-K_α (λ=0.154056 nm) radiation, operating at 45 kV and 30 mA, with step size of 2θ=0.017 deg. The peaks in the diffraction patterns were identified using International Committee for Diffraction Data (ICDD) database in PCPDFWIN software. The phase distribution and compositional analyses of suction cast and heat treated samples were observed using the scanning electron microscope (Inspect F) equipped with an energy-dispersive spectrometer. The micrographs were obtained in the back scattered electron (BSE) imaging mode to reveal the different phases in the microstructure due to atomic number (Z) contrast. In addition, the composition of different phases in the microstructure was measured by using energy dispersive X-ray spectroscopic (EDS) analysis. Transmission electron microscopy (TEM) observations were carried out using a 200 kV (TEM, FEI $G^{2,}$ 20UT) microscope. The specimen for TEM observation was prepared by the standard preparation technique, which includes cutting of 3-mm disks, grinding, dimpling, and subsequent ion-milling at 5 kV at an angle of 5° until perforation occurred.

Isothermal hot compression tests of the cylindrical samples (ϕ=10 mm and aspect ratio of 1.5:1) were carried out using Gleeble 3800® thermo mechanical simulator at different deformation temperatures of 800 °C (1073 K), 900 °C (1173 K), 950 °C (1223 K) and 1000 °C (1273 K) with constant strain rates of 10^{-1}, 10^{-2} and 10^{-3} s^{-1}. A graphite sheet was placed in between sample ends and anvil (along with Ni paste) to ensure sufficient lubrication during each test in order to minimize friction. All the samples were heated by direct resistance heating system at a heating rate of 10 K/s from room temperature to the testing temperature and soaked for 5 min at that temperature to obtain the uniform distribution of temperature in the entire sample. The variation of the deformation temperature should be controlled with 2° C error limit. All the tests were conducted in the argon atmosphere. The samples were deformed to a total true strain of ε~0.7 that corresponds to 50% reduction in the height of the sample and were quenched with distilled water to freeze the microstructure. During the process of compression, the flow stress was recorded as a function of true strain for each strain rate and deformation temperature. The microstructural analysis of the deformed samples was carried out on cross-sections which were cut along the compression axis.

3. Results and discussion

3.1. Structural characterization

The XRD patterns of the suction cast (ϕ=10 mm) multicomponent $Co_{20}Cu_{20}Fe_{20}Ni_{20}Ti_{20}$ eutectic high entropy alloy (HEA) is shown in Fig. 1a. The XRD pattern shows the intense diffraction peaks corresponding to fcc (α_1) ($Fm\bar{3}m$), fcc (α_2) ($Fm\bar{3}m$), bcc (β) ($Im\bar{3}m$) solid solution phases and the Laves phase (Ti_2(Ni, Co)-type ($FD\bar{3}m$)).

3.2. Microstructural characterization

A detailed SEM characterization of the multicomponent $Co_{20}Cu_{20}Fe_{20}Ni_{20}Ti_{20}$ eutectic high entropy alloy (HEA) was carried out. A representative SEM micrograph of the alloys is shown in Fig. 1b, which illustrate the various phases formed in this equimolar alloy. The different phases in the microstructure are marked based on the EDS compositional measurements. The multicomponent $Co_{20}Cu_{20}Fe_{20}Ni_{20}Ti_{20}$ eutectic HEA shows the presence of different phases i.e. Co-rich solid solution (α_2) phase with light gray contrast, Ti-rich solid solution (β) phase (black contrast), Cu-rich solid solution (α_1) phase with white contrast and Ti_2(Ni, Co)-type Laves phase with dark-gray contrast. The eutectic matrix is between the α_1-phase and Ti_2(Ni, Co)-type Laves phase. The volume fraction of Ti-rich solid solution (β) phase (black contrast)

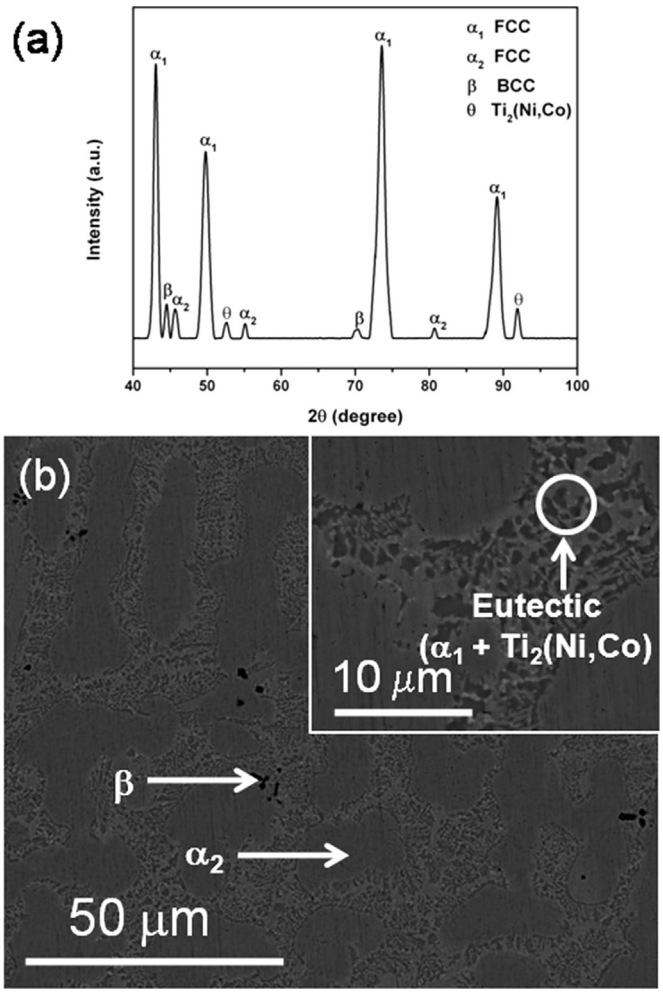

Fig. 1. (a) XRD pattern and (b) BSE-SEM micrograph (α_1: Cu-rich solid solution, α_2: Co-rich solid solution and β: Ti-rich solid solution) of multicomponent $Co_{20}Cu_{20}Fe_{20}Ni_{20}Ti_{20}$ eutectic high entropy alloy.

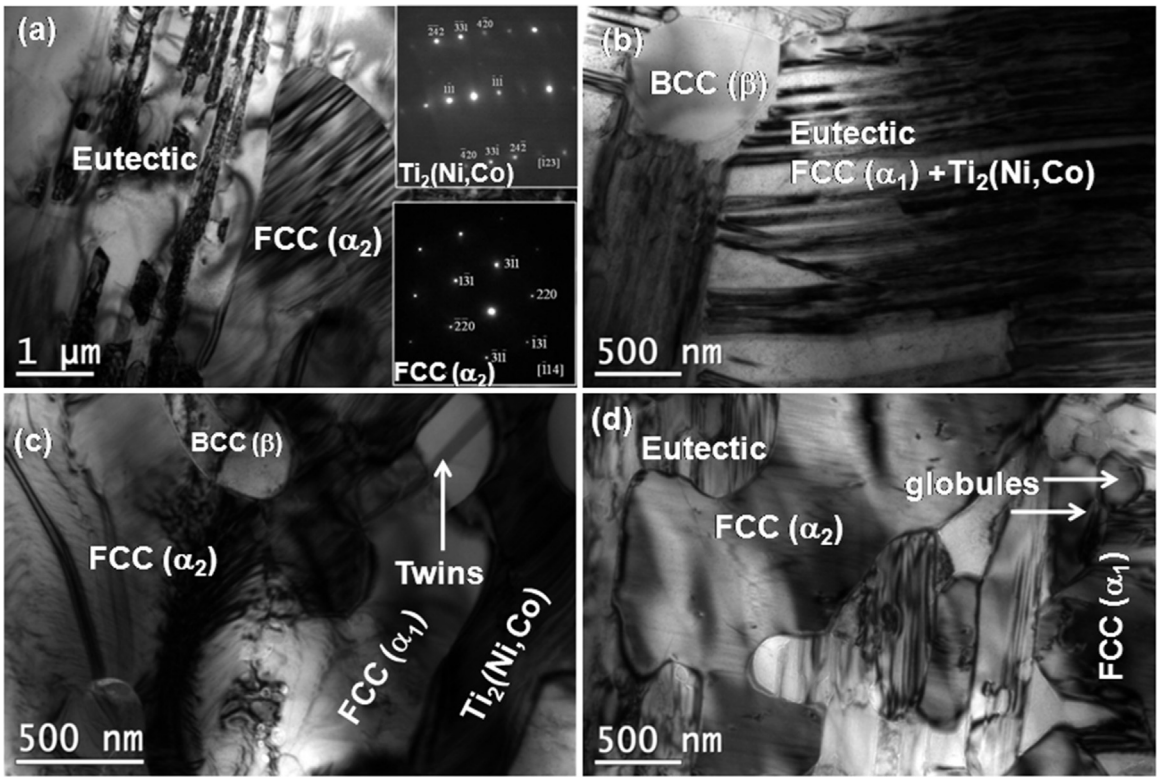

Fig. 2. TEM micrograph of the suction cast ($\phi = 10$ mm) multicomponent $Co_{20}Cu_{20}Fe_{20}Ni_{20}Ti_{20}$ eutectic high entropy alloy, annealed at 1223 K and soaked for 5 min, followed by quenching distilled water, revealing detailed microstructural features (a) FCC (α_2) and eutectic, (b) BCC (β) and eutectic, (c) Twins, defects in FCC (α_1) phase, and (d) presence of small crystals in FCC (α_1) phase.

and Co-rich solid solution (α_2) phase with light gray contrast are $1.6 \pm 0.3\%$ and $77.3 \pm 1.5\%$ respectively, whereas volume fraction of the eutectic (Cu-rich solid solution (α_1) plus Ti_2(Ni, Co)-type Laves phase (θ)) is $21.1 \pm 0.6\%$.

The suction cast ($\phi = 10$ mm) multicomponent $Co_{20}Cu_{20}Fe_{20}Ni_{20}Ti_{20}$ eutectic HEA was annealed at 950 °C for 5 min to obtain a uniform distribution of temperature throughout the specimen, followed by quenching with distilled water to freeze the microstructure. A detailed TEM characterization of the annealed Co-Cu-Fe-Ni-Ti eutectic HEA was carried out. The representative TEM micrographs of the annealed sample are shown in Fig. 2 to elucidate the fine scale microstructural features. The phases in the microstructure are identified by analyzing the obtained selected area diffraction pattern. The microstructure reveals the presence of eutectic between fcc (α_1) and Ti_2(Ni, Co)-type Laves phases as well as bcc (β) and fcc (α_2) dendritic phases (Fig. 2a and b). It is also observed that fcc (α_1) phase is twinned, defective in nature (Fig. 2c) and also contains large number of small crystals (Fig. 2d).

4. Compressive mechanical behaviour at elevated temperature

The true stress-strain curves of the multicomponent Co-Cu-Fe-Ni-Ti eutectic HEA at different temperatures (800 °C (1073 K), 900 °C (1173 K), 950 °C (1223 K) and 1000 °C (1273 K)) and at different strain rates (10^{-1}, 10^{-2} and 10^{-3} s^{-1}) were obtained for the suction cast cylinder samples with diameter (ϕ) = 10 mm having an aspect ratio of 1.5:1.

4.1. Flow behaviour of Co-Cu-Fe-Ni-Ti eutectic HEA

Fig. 3a and b show the true stress (σ) – true strain (ε) curves of the multicomponent $Co_{20}Cu_{20}Fe_{20}Ni_{20}Ti_{20}$ eutectic HEA at various testing temperatures of 800 °C (1073 K), 900 °C (1173 K), 950 °C (1223 K) and 1000 °C (1273 K), and at a highest strain rate of 10^{-1} and at lowest strain rate of 10^{-3} s^{-1}, respectively. The DSC and time-temperature plot (Fig. S1 in Supplementary section) of eutectic HEA shows endothermic peaks > 1000 °C, 1024 °C, 1090 °C and 1095 °C, which correspond to the melting temperature of eutectic, bcc (β) and fcc (α_2) phases, respectively. Hence, it is clear that there is no phase transformation during the deformation of the studied eutectic alloys up to 1000 °C. It is also evident from Fig. 3 that the flow stress decreases with increase in temperature at a given strain rate ($\dot{\varepsilon}$). Similarly, the flow stress (σ) increases with increase in the strain rate at a given deformation temperature. The flow stress reaches a maximum value at a critical strain followed by a softening that continues up to a strain of 0.7, except at 1223–1273 K and at 10^{-3} s^{-1}, where there seems to be steady state beyond a strain of 0.3 [28, 29]. It is interesting to note that the drop in flow stress from peak stress to softening stage is lower at higher strain rates (10^{-1} s^{-1}) as compared to that at lower strain rate of 10^{-3} s^{-1}. During deformation, at first the matrix i.e. fcc (α_2) and bcc (β) (~79%) in the microstructure takes the load and deforms extensively up to the yield point of the matrix and subsequently the load is transferred to the interdendritic phases (~21%) i.e. eutectic phases (fcc (α_1) plus Ti_2(Ni, Co)-type Laves phase).

It is observed that the flow curves of the multicomponent eutectic HEA exhibit globulization or dynamic recrystallization and propagation of cracks at different combinations of temperature and strain rate. However, the flow curves at the lowest strain rate ($\dot{\varepsilon}$) and at highest deformation temperature show continuous flow softening which is attributed to globulization or dynamic recrystallization. The large drop in stress value after yield point could be due to dynamic recrystallization, which in general is attributed to softening during hot deformation. The dynamic globulization kinetics in the Ti–6Al–4 V alloy with colony microstructure was extensively studied by Semiatin et al. [29].

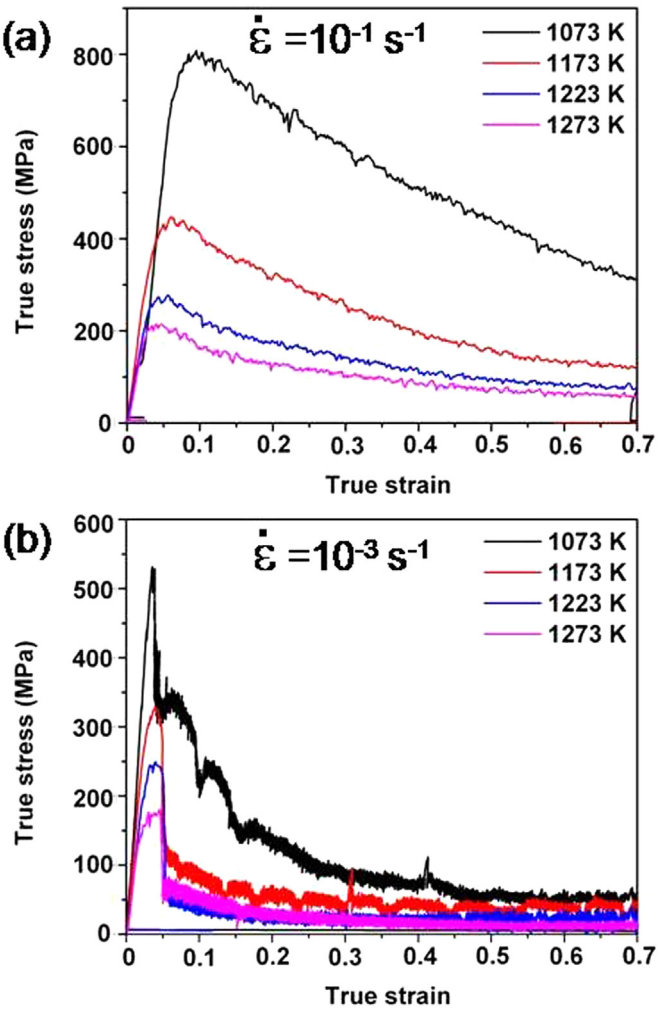

Fig. 3. True stress – true strain plots at different temperatures and strain rates of (a) 10^{-1} and (b) $10^{-3}\,s^{-1}$.

It is interesting to note that the serrations are prominent at higher strain rate ($10^{-1}\,s^{-1}$), and the amplitude of serrations is increasing with decrease in the temperature. In contrast, at lower strain rate ($10^{-3}\,s^{-1}$), the serrations are prominently visible at lower temperature but not at higher temperature. Although, the specific rationale for serrations is not very clear at this moment, the following analysis is a plausible explanation. Due to more number of phases (α_1, α_2, β and eutectic phase), the deformation behaviour of this HEA appears to be complex. It is important to note that the eutectic (α_1-phase and Ti_2(Ni, Co)-type Laves phase) is harder as compared to other phases in the microstructure of the present studied alloy because of its lamellar morphology, which is characterized by interlamellar spacing (λ). Usually, such high strength of eutectic is attributed to Hall-Petch type mechanism [30] i.e. $\sigma_y = \sigma_0 + k_H\,\lambda^{(-1/2)}$; where σ_y is the yield strength of the material, σ_0 is the friction stress, and k_H is Hall-Petch slope. In general, interlamellar spacing (λ) is directly proportional to the diffusion coefficient (D) [31]. Since diffusion is known to be sluggish in high entropy alloys [13], interlamellar spacing (λ) will be smaller. Therefore, the strength of eutectic will be more. However, the fcc (α_2) phase ($77.3 \pm 1.5\%$) is the softer phase due to the presence of large number of active slip systems. Among these phases, the softer phase at a specific temperature and strain rate deforms first. While this phase becomes softer due to changes within its microstructure, the other hard phases within the microstructure bears the maximum deformation and hence the stress goes up. This process continues until the deformed microstructure becomes uniform throughout. Thus, it is interesting to note that amplitude of the serrations is decreased at higher strains, which is consistent with the above analysis.

Zhang et al. [32] reported the serration behaviour in the materials, is attributed to the different flow units such as dislocations, twins, grain boundaries etc., and dependence of flow unit with temperature and strain rate. Antonaglia et al. [33] reported temperature effects on the serration behaviour of MoNbTaW and $Al_{0.5}$CoCrCuFeNi alloys through compression experiments at constant strain rate. The serration characteristics for the present $Co_{20}Cu_{20}Fe_{20}Ni_{20}Ti_{20}$ eutectic HEA can also be understood based on the temperature and strain rate. It is clear that the serration behaviour i.e. the amplitude of serration decreases with increase of temperature at a particular strain rate (Fig. 3). One possible reason could be that the thermal vibration energy for pinning the solute atom is more at high temperature i.e. the pinning effect of solute atom around dislocation is lesser at high T. Since the sole products of HEAs are considered as the solid solution phases, hence each element can be considered as solute atoms. The serrations in the flow curve start appearing after some amount of plastic strain, which is necessary for enhancing the solutes diffusion to affect the dislocations. It is also evident from Fig. 3 that the amplitude of serrations is more at lower strain rate i.e. the amplitude of serration at a strain rate of $10^{-3}\,s^{-1}$ is high as compared to strain rate of $10^{-1}\,s^{-1}$ for a particular temperature of 1073 K. Since atoms get more time to lock the dislocation at lower strain rate, the amplitude is higher. To summarize the flow behaviour, the combination of testing temperature and strain rate play a vital role in specific deformation characteristics.

Further, it is reported in the literature [34] that there are mainly three different types of serration statistics in the flow curve of the materials, such as Type A or locking type of serrations, which are characterized by rise and drop of stress with discontinuous frequency in the general level of stress-strain plot, Type B serrations, which are manifested by means of rise and drop of stress in quick succession in the stress-strain curve and finally, Type C or unlocking type of serrations is due to stress drop below the general level of stress–strain curve. It is important to note that the type of serrations in the plastic regime of flow curve (Fig. 3) of the present eutectic HEA was found to vary from Type A (1073 K), to Type A+B (1173 K, 1223 K, 1273 K) for a given strain rate of $10^{-1}\,s^{-1}$, whereas at strain rate of $10^{-3}\,s^{-1}$, the type of serrations changes from Type A+B (1073 K, 1173 K) to Type B (1223 K, 1273 K). Thus, it is clear that the serration characteristics change from Type A to Type B with various combinations of temperature and strain rate.

5. Constitutive mechanical behaviour of multicomponent $Co_{20}Cu_{20}Fe_{20}Ni_{20}Ti_{20}$ eutectic HEA

The flow stress of a material (σ) is correlated with the strain (ε), strain rate ($\dot{\varepsilon}$) and temperature (T) by means of the constitutive equations. The constants in the constitutive equations are derived from the test data and validated with the experimentally determined values.

The flow curves at peak stress values in the stress-strain responses are expressed by means of power law equation:

$$\dot{\varepsilon} = A\sigma^{n}\exp\left[\frac{-Q}{RT}\right] \quad (1)$$

where $\dot{\varepsilon}$ is the strain rate, Q is the activation energy corresponding to the deformation mechanisms occurring during hot working, σ is the peak or steady state stress, A is the material constant which is experimentally determined, n is stress exponent, R is universal gas

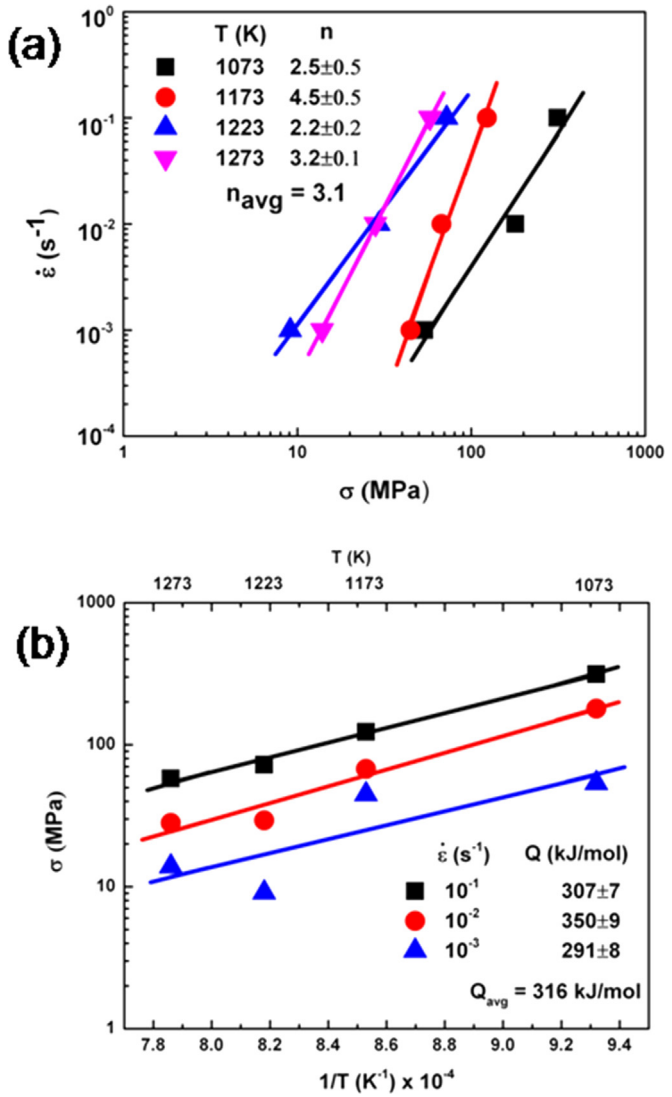

Fig. 4. (a) plot between $\dot{\varepsilon}$ and σ and (b) σ and 1/T; used for calculating the activation energy (Q). It is important to note that the flow stress data is taken at strain (ε)=0.7; $\dot{\varepsilon}$ and σ are in logarithmic scale.

constant (=8.314 J/mol-K) and T is the temperature in Kelvin. The activation energy (Q) is the physical parameter, which signifies the plastic deformability. The Q-value can also be calculated as follows.

Taking logarithm of both sides of power law Eq. (1), we get

$$\log\dot{\varepsilon} = \log A + n\log\sigma - \frac{Q}{2.303RT} \quad (2)$$

The slope of $\log\dot{\varepsilon}$ vs $\log\sigma$ (i.e. $\frac{\partial\log\dot{\varepsilon}}{\partial\log\sigma}$) at different deformation temperature T gives stress exponent value (n), whereas the slope of $\log\sigma$ and 1/T (i.e. $\frac{\partial\log\sigma}{\partial(1/T)}$) at different strain rate ($\dot{\varepsilon}$) gives the activation energy (Q).

The activation energy (Q) for the multicomponent $Co_{20}Cu_{20}Fe_{20}Ni_{20}Ti_{20}$ eutectic HEA was calculated at a strain of 0.7. The plot between $\log\dot{\varepsilon}$ and $\log\sigma$ at different deformation temperature T, $\log\sigma$ and 1/T at different strain rates ($\dot{\varepsilon}$) are shown in Fig. 4a and b, respectively. The average value of the slopes of $\log\dot{\varepsilon}$ vs $\log\sigma$ at different T (i.e. the stress exponent n) is calculated as 3.1. Thus, the activation energy (Q) is estimated as 318 kJ/mol, 277 kJ/mol and 316 kJ/mol at a true strain (ε)=0.1, 0.2 and 0.7, respectively. Therefore, the constitutive equation which describes the flow stress of the multicomponent $Co_{20}Cu_{20}Fe_{20}Ni_{20}Ti_{20}$ eutectic HEA as a function of $\dot{\varepsilon}$ and T at strain (ε) of 0.7 can be written as:

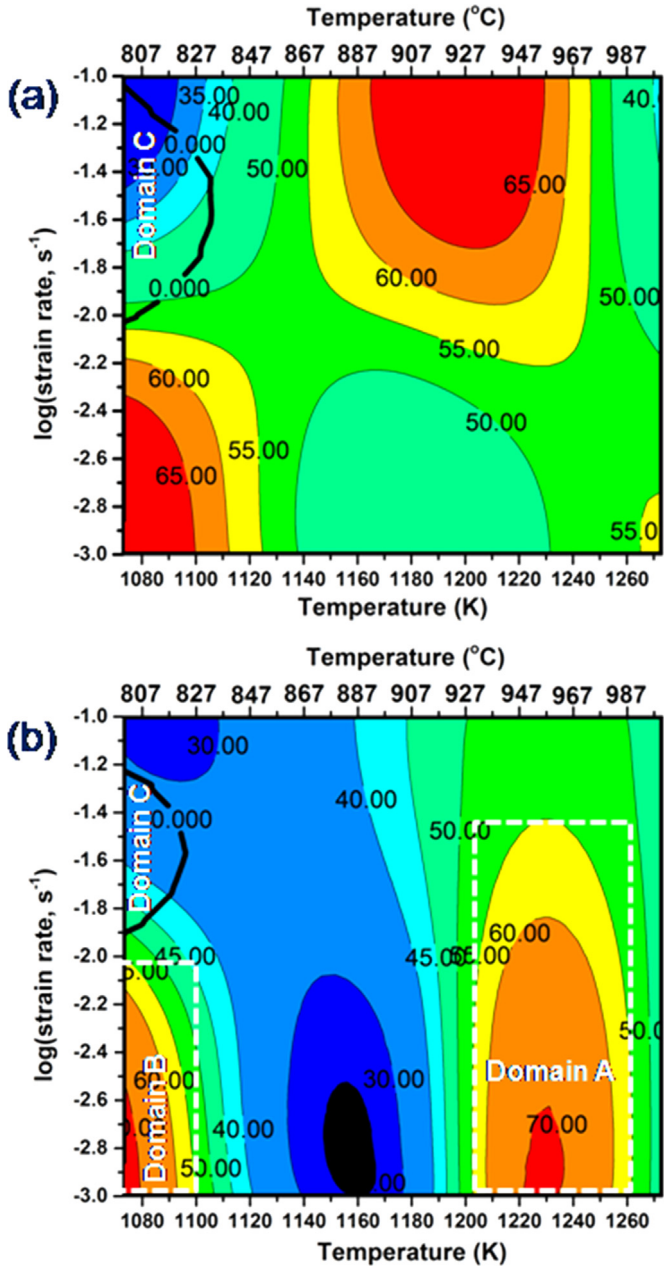

Fig. 5. 2-D contour maps of the efficiency of power dissipation at a true strain of (a) 0.2 and (b) 0.7 and Domain C corresponds to the instability map of the alloy delineating unstable and stable regime at a true strain of (a) 0.2, and (b) 0.7.

$$\dot{\varepsilon} \sim \sigma^{3.1}\exp\left(-\frac{316000}{RT}\right) \quad (3)$$

However, it is important to note that this constitutive equation for the studied $Co_{20}Cu_{20}Fe_{20}Ni_{20}Ti_{20}$ eutectic HEA describes the correlation between the strain rate and the stress within this temperature range. Roy et al. [35] reported the activation energy in the range 265–370 kJ/mol for commercial Ti–6Al–4 V with α colony microstructure. And the hot deformation behaviour of this alloy at different temperatures and strain rates is explained on the basis of different factors such as dynamic recovery, globularization, dynamic recrystallization (DRx), grain boundary sliding etc. According to power law equation, the activation energy for the present eutectic HEA is ~316 kJ/mol and the stress exponent value is ~3. Since eutectic HEAs are new class of materials and all elements are considered as major substitutional solutes, the

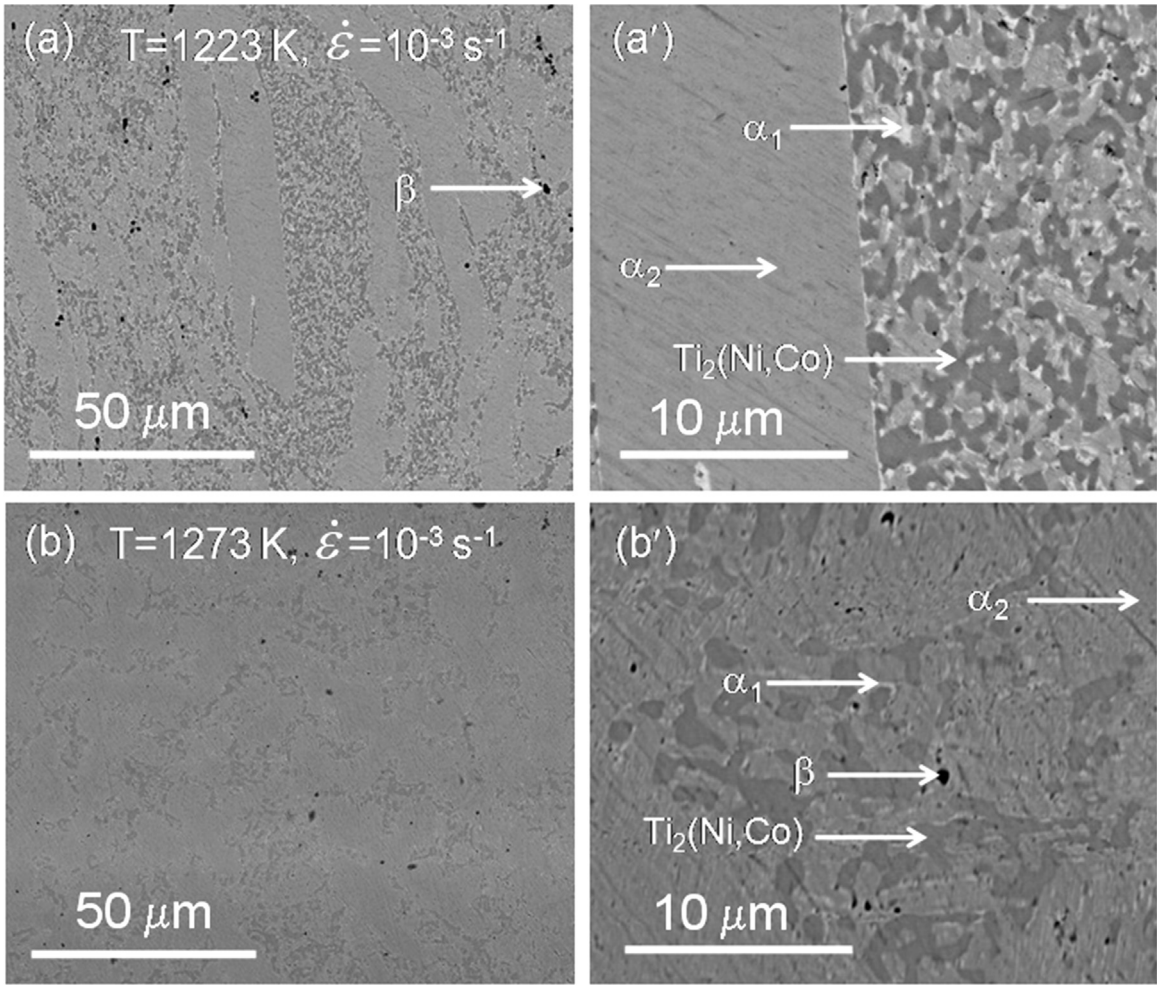

Fig. 6. BSE-SEM micrograph of multicomponent $Co_{20}Cu_{20}Fe_{20}Ni_{20}Ti_{20}$ eutectic high entropy alloy, deformed at (a) 1223 K and (b) 1273 K with strain rates of 10^{-3} s^{-1}. (α_1: Cu-rich solid solution, α_2: Co-rich solid solution and β: Ti-rich solid solution, Left: low magnification and Right: corresponding high magnification).

activation energy for the interaction of the solute atoms with dislocations consist of combination of both energy for the formation of vacancy and also energy for solute migration. Thus, substitutional solutes are considered as one of the possible rate controlling factor for the occurrence of serrations in the flow curve.

6. Generation of processing map

The processing map can provide guidelines about safe secondary processing window of strain rate and temperature based on the power dissipation efficiency and instability domains. Thus, the power dissipation efficiency and deformation instability maps for the multicomponent $Co_{20}Cu_{20}Fe_{20}Ni_{20}Ti_{20}$ eutectic HEA were generated using dynamic material modeling (DMM). This model assumes that plastic flow during hot working is a dynamic, nonlinear and irreversible phenomena [36,37]. In general, the hot working of the materials is characterized by the constitutive equations which relates the flow stress (σ) to strain (ε), strain rate ($\dot{\varepsilon}$) and temperature (T). The strain rate sensitivity parameter (m) and the efficiency of power dissipation (η) are key parameters in DMM. The DMM model assumes that the total instantaneous power absorbed by the work piece from the equipment is dissipated by means of two ways: (a) temperature rise i.e. dissipater content G, which is the power dissipated via plastic deformation and, (b) microstructural change i.e. dissipater co-content, J, which is dissipated through different metallurgical processes such as dynamic recovery, dynamic recrystallization, flow localization, shear band formation and phase transformations etc.

The strain rate sensitivity parameter (m) is given by the following equation:

$$m=\frac{d\sigma}{d\varepsilon}=\left(\frac{\partial \ln\sigma}{\partial \ln\dot{\varepsilon}}\right)_T \quad (4)$$

For an ideal linear power dissipater, m=1 and $J_{max} = \sigma\dot{\varepsilon}/2$. Whereas for a non-linear power dissipater, the efficiency of power dissipation is given by the following equation:

$$\eta = \frac{J}{J_{max}} = \frac{2m}{m+1} \quad (5)$$

The condition for instability [38] is represented by a dimensionless instability parameter ($\xi(\dot{\varepsilon})$)that can be obtained as:

$$\xi(\dot{\varepsilon}) = \left[\frac{\partial \ln(m/m+1)}{\partial \ln\dot{\varepsilon}}\right]+m < 0 \quad (6)$$

The variation of dimensionless instability parameter ($\xi(\dot{\varepsilon})$) with strain rate ($\dot{\varepsilon}$) and temperature (T) constitutes an instability map in the deformation processing map [38]. This dimensional parameter represents that the material exhibits flow instabilities when the $\xi(\dot{\varepsilon})$ is negative.

The iso-efficiency contour map generated for multicomponent $Co_{20}Cu_{20}Fe_{20}Ni_{20}Ti_{20}$ eutectic HEA based on the DMM model at different strain values of 0.2 and 0.7 are shown in Fig. 5a and b,

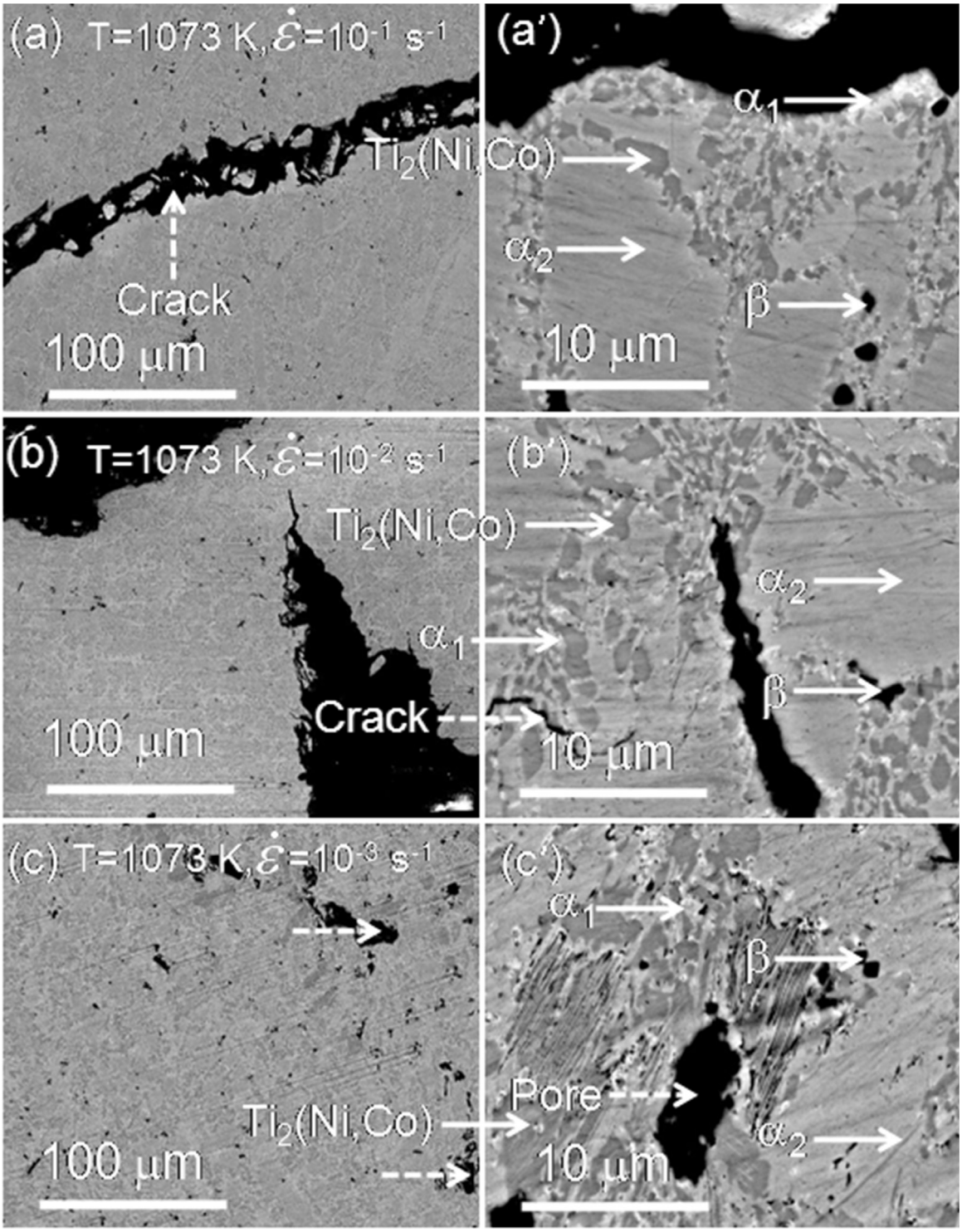

Fig. 7. BSE-SEM micrograph of multicomponent $Co_{20}Cu_{20}Fe_{20}Ni_{20}Ti_{20}$ eutectic high entropy alloy, deformed at 1073 K with strain rates of (a) 10^{-1} s^{-1}, (b) 10^{-2} s^{-1}and (c) 10^{-3} s^{-1}. (α_1: Cu-rich solid solution, α_2: Co-rich solid solution and β: Ti-rich solid solution, Left: low magnification and Right: corresponding high magnification).

Table 1
Different domains in the processing maps and corresponding microstructural features.

	Strain rate (s^{-1})	Temperature (K)	Efficiency (η) %	Microstructural features
Domain A	10^{-3}–10^{-1}	1203–1263	50–70	Uniform distribution of phases in the microstructure
Domain B	10^{-3}–10^{-2}	1073–1103	50–70	Pores, Localized flow
Domain C (Instability regions)	10^{-2}–10^{-1}	1073–1093	30–40	Large Cracks, small pieces near cracks

respectively. The negative regime of flow instability parameter which represents the flow instability is also superimposed on this efficiency contour map, and is shown as Domain C. It is important to note that the materials flow is microstructurally unstable in the instability regime. It is clear from Fig. 5b (processing map for 0.7 strain) that high value of η (~50–70%) is observed in the temperature range of 930–990 °C (1203–1263 K) and in the strain rate range of 10^{-3}–10^{-1} s^{-1} (Domain A) for the present multicomponent $Co_{20}Cu_{20}Fe_{20}Ni_{20}Ti_{20}$ eutectic HEA. Similarly, there is another region with high η is represented as Domain B (η~50–70%) in the temperature range 800–830 °C (1073–1103 K) and strain rate range of 10^{-3}–10^{-2} s^{-1}. In general, in many of the metallic alloys, it has been reported that higher peak efficiency (η) leads to the better workability of materials [38]. However, flow localization such as shear band formation can also have higher efficiency, but not ideal for thermo mechanical processing. According to the instability map, the instability parameter $\xi(\dot{\varepsilon})$ at a true strain of 0.7 is found to be in the temperature (T) range 800–820 °C (1073–1093 K) and strain rate ($\dot{\varepsilon}$) range of 10^{-2}–10^{-1} s^{-1} (marked as Domain C). Thus, the region of low temperature and high strain rate is considered as the unstable region, and hence this regime should be avoided to do thermo mechanical processing. Further, it is important to note that higher value of peak efficiency (η) and positive value of instability parameter correspond to the better workability of materials. It is also observed that the efficiency (η) of the present multicomponent eutectic HEA is better as compared to the efficiency of HEA reported by Nayan and coworkers [26,27]. The comparison of Fig. 5a and b suggests that as the deformation accumulates in the specimen, some regions of higher efficiency vanish, and in parallel, some lower efficient regimes have become higher efficient regimes. For example, at 0.2 strain, there is a region of η~50–65% in the temperature range of 1140–1240 K in the high strain rate range of 10^{-2}–10^{-1} s^{-1}. However, this region vanishes at strain of 0.7. Thus it is important to note that processing map generated at higher strains is vital in order to identify the safe domain for secondary thermo mechanical processing.

The microstructural characterization of the deformed multicomponent Co-Cu-Fe-Ni-Ti eutectic HEA at different strain rates and temperatures was carried out to correlate with the observations drawn from the deformation maps and instability maps. The deformed microstructures corresponding to the various domains of processing maps are given in Figs. 6 and 7. Table 1 shows the different domains in the deformation processing maps (Fig. 5) and corresponding characteristic microstructural features. Fig. 7 shows the microstructure of the instability region (Domain C) i.e. microstructure of deformed sample tested at 1073 K (800 °C) at strain rate of 10^{-1} s^{-1} and 10^{-2} s^{-1}, showing the cracks. It is clear from Fig. 7b that cracks pass through the eutectic regions and are moved around α_2 phase. This is well correlated with the conclusion drawn from the instability processing map (Domain C in Fig. 5). It was reported [38] that the instability mechanism is attributed to the presence of cracking, adiabatic shear banding or localized plastic flow. It is also found that the sample deformed at 1073 K (800 °C) and 10^{-3} s^{-1} (Domain B) shows large amount of porosity and localized plastic flow near the pores. However, in contrast, the microstructure of sample deformed at temperature 950, 1000 °C (Domain A in Fig. 5) and strain rate of 10^{-1} s^{-1}, 10^{-2} s^{-1} and 10^{-3} s^{-1} shows free of cracks, voids and hence corroborates well with predictions from the processing map and hence considered as the stable region. As evident from Fig. 6, the original microstructure of the as-cast sample was replaced by highly worked and reconstituted microstructure after deformed at 950 and 1000 °C with strain rate of 10^{-3} s^{-1}. Further, a uniform distribution of phases was also observed in the microstructure. The dynamic recrystallization or globulization in the eutectics, in particular in fcc (α_1) phase was observed in the deformation microstructure of sample thermo mechanically processed at 950 and 1000 °C at a strain rate of 10^{-3} s^{-1}. Therefore, for multicomponent $Co_{20}Cu_{20}Fe_{20}Ni_{20}Ti_{20}$ eutectic HEA investigated in the present study, T=930–990 °C (1203–1263 K) and strain rate range of 10^{-3} s^{-1}–10^{-1} s^{-1} (Domain A) is the optimum thermo-mechanical processing (TMP) window for any further secondary processing.

7. Conclusions

The hot working characteristics of the multicomponent $Co_{20}Cu_{20}Fe_{20}Ni_{20}Ti_{20}$ eutectic HEA was investigated by conducting hot compression tests in a Gleeble thermo mechanical simulator in the temperature range 800–1000 °C and in the strain rate range of 10^{-3}–10^{-1} s^{-1}. The following conclusions can be drawn based on the results and discussion presented above with respect to multicomponent eutectic HEA.

1. The average activation energy (Q) of the multicomponent $Co_{20}Cu_{20}Fe_{20}Ni_{20}Ti_{20}$ eutectic HEA is estimated to be 316 kJ/mol.
2. The amplitude of serrations for the investigated $Co_{20}Cu_{20}Fe_{20}Ni_{20}Ti_{20}$ eutectic HEA decreases with increase of temperature at a particular strain rate, whereas the amplitude of serrations is higher with a decrease of strain rate at a given temperature.
3. The microstructural instability of the deformation of material has been observed at deformation temperature (T) range 800–820 °C (1073–1093 K) and strain rate ($\dot{\varepsilon}$) range 10^{-2} s^{-1}–10^{-1} s^{-1}.
4. The optimum thermo-mechanical processing (TMP) parameters are T=930–990 °C (1203–1263 K) and strain rate in the range of 10^{-3} s^{-1}–10^{-1} s^{-1}.

Acknowledgements

One of the authors (S.S.) would like to thank IIT Madras for the post-doctoral fellowship that has made this study possible.

Appendix A. Supplementary material

Supplementary data associated with this article can be found in the online version at http://dx.doi.org/10.1016/j.msea.2016.04.006.

References

[1] B.S. Murty, J.W. Yeh, S. Ranganthan, High Entropy Alloys, Elsevier, 2014.
[2] Y. Zhang, T.T. Zuo, Z. Tang, M.C. Gao, K. a Dahmen, P.K. Liaw, et al., Microstructures and properties of high-entropy alloys, Prog. Mater. Sci. 61 (2014) 1–93, http://dx.doi.org/10.1016/j.pmatsci.2013.10.001.
[3] J.W. Yeh, S.K. Chen, S.J. Lin, J.-Y. Gan, T.S. Chin, T.T. Shun, C.H. Tsau, S.Y. Chang, Nanostructured high-entropy alloys with multiple principal elements: novel alloy design concepts and outcomes, Adv. Eng. Mater. 6 (2004) 299–303, http://dx.doi.org/10.1002/adem.200300567.
[4] B. Cantor, I.T.H. Chang, P. Knight, A.J.B. Vincent, Microstructural development in equiatomic multicomponent alloys, Mater. Sci. Eng. A. 375–377 (2004) 213–218, http://dx.doi.org/10.1016/j.msea.2003.10.257.
[5] J.W. Yeh, S.J. Lin, T.S. Chin, J.Y. Gan, S.K. Chen, T.T. Shun, C.H. Tsau, S.Y. Chang, Formation of simple crystal structures in Cu-Co-Ni-Cr-Al-Fe-Ti-V alloys with multiprincipal metallic elements, Metall. Mater. Trans. A. 35 (2004) 2533–2536, http://dx.doi.org/10.1007/s11661-006-0234-4.
[6] S. Praveen, B.S. Murty, R.S. Kottada, Alloying behavior in multi-component AlCoCrCuFe and NiCoCrCuFe high entropy alloys, Mater. Sci. Eng. A. 534 (2012) 83–89, http://dx.doi.org/10.1016/j.msea.2011.11.044.
[7] S. Guo, C. Ng, C.T. Liu, Sunflower-like solidification microstructure in a near-eutectic high-entropy alloy, Mater. Res. Lett. 1 (2013) 228–232, http://dx.doi.org/10.1080/21663831.2013.844737.

[8] R. Sriharitha, B.S. Murty, R.S. Kottada, Phase formation in mechanically alloyed Al xCoCrCuFeNi (x=0.45, 1, 2.5, 5 mol) high entropy alloys, Intermetallics 32 (2013) 119–126, http://dx.doi.org/10.1016/j.intermet.2012.08.015.
[9] S. Mridha, S. Samal, P.Y. Khan, K. Biswas, Govind, Processing and consolidation of nanocrystalline Cu-Zn-Ti-Fe-Cr high-entropy alloys via mechanical alloying, Metall. Mater. Trans. A Phys. Metall. Mater. Sci. 44 (2013) 4532–4541, http://dx.doi.org/10.1007/s11661-013-1824-6.
[10] R. Sriharitha, B.S. Murty, R.S. Kottada, Alloying, thermal stability and strengthening in spark plasma sintered AlxCoCrCuFeNi high entropy alloys, J. Alloy. Compd. 583 (2014) 419–426, http://dx.doi.org/10.1016/j.jallcom.2013.08.176.
[11] S. Praveen, J. Basu, S. Kashyap, R.S. Kottada, Exceptional resistance to grain growth in nanocrystalline CoCrFeNi high entropy alloy at high homologous temperatures, J. Alloy. Compd. 662 (2016) 361–367, http://dx.doi.org/10.1016/j.jallcom.2015.12.020.
[12] K.Y. Tsai, M.H. Tsai, J.W. Yeh, Sluggish diffusion in Co-Cr-Fe-Mn-Ni high-entropy alloys, Acta Mater. 61 (2013) 4887–4897, http://dx.doi.org/10.1016/j.actamat.2013.04.058.
[13] D.L. Beke, G. Erdélyi, On the diffusion in high-entropy alloys, Mater. Lett. 164 (2016) 111–113, http://dx.doi.org/10.1016/j.matlet.2015.09.028.
[14] O.N. Senkov, G.B. Wilks, J.M. Scott, D.B. Miracle, Mechanical properties of Nb25Mo25Ta25W25 and V20Nb20Mo20Ta20W20 refractory high entropy alloys, Intermetallics 19 (2011) 698–706, http://dx.doi.org/10.1016/j.intermet.2011.01.004.
[15] A.K. Mishra, S. Samal, K. Biswas, Solidification behaviour of Ti-Cu-Fe-Co-Ni high entropy alloys, Trans. Indian Inst. Met. 65 (2012) 725–730, http://dx.doi.org/10.1007/s12666-012-0206-x.
[16] S. Samal, S. Mohanty, A.K. Misra, K. Biswas, B. Govind, Mechanical behavior of novel suction cast Ti-Cu-Fe-Co-Ni high entropy alloys, Mater. Sci. Forum 790–791 (2014) 503–508, http://dx.doi.org/10.4028/www.scientific.net/MSF.790-791.503.
[17] S. Mohanty, S. Samal, A. Tazuddin, C.S. Tiwary, N.P. Gurao, K. Biswas, Effect of processing route on phase stability in equiatomic multicomponent Ti20-Fe20Ni20Co20Cu20 high entropy alloy, Mater. Sci. Technol. 31 (2015) 1214–1222, http://dx.doi.org/10.1179/1743284715Y.0000000024.
[18] Y. Liu, R. Hu, J. Li, H. Kou, H. Li, H. Chang, H. Fu, Deformation characteristics of as-received Haynes230 nickel base superalloy, Mater. Sci. Eng. A 497 (2008) 283–289, http://dx.doi.org/10.1016/j.msea.2008.07.052.
[19] J.K. Fan, H.C. Kou, M.J. Lai, B. Tang, H. Chang, J.S. Li, Characterization of hot deformation behavior of a new near beta titanium alloy: Ti-7333, Mater. Des. 49 (2013) 945–952, http://dx.doi.org/10.1016/j.matdes.2013.02.044.
[20] I. Sen, R.S. Kottada, U. Ramamurty, High temperature deformation processing maps for boron modified Ti-6Al-4V alloys, Mater. Sci. Eng. A 527 (2010) 6157–6165, http://dx.doi.org/10.1016/j.msea.2010.06.044.
[21] M.A. Jabbari-Taleghani, J.M. Torralba, Hot workability of nanocrystalline AZ91 magnesium alloy, J. Alloy. Compd. 595 (2014) 1–7, http://dx.doi.org/10.1016/j.jallcom.2014.01.091.
[22] L. Wang, G. Fang, S. Leeflang, J. Duszczyk, J. Zhou, Investigation into the hot workability of the as-extruded WE43 magnesium alloy using processing map, J. Mech. Behav. Biomed. Mater. 32 (2014) 270–278, http://dx.doi.org/10.1016/j.jmbbm.2014.01.011.
[23] Y.Q. Ning, Z.K. Yao, Z. Yang, H.Z. Guo, M.W. Fu, Flow behavior and hot workability of FGH4096 superalloys with different initial microstructures by using advanced processing maps, Mater. Sci. Eng. A 531 (2012) 91–97, http://dx.doi.org/10.1016/j.msea.2011.10.039.
[24] Y. Wang, L. Zhen, W.Z. Shao, L. Yang, X.M. Zhang, Hot working characteristics and dynamic recrystallization of delta-processed superalloy 718, J. Alloy. Compd. 474 (2009) 341–346, http://dx.doi.org/10.1016/j.jallcom.2008.06.079.
[25] S.V.S.N. Murty, B.N. Rao, B.P. Kashyap, Hot Working Characteristics of Powder Metallurgy Nimonic AP-1 superalloy, 44, 2001, pp. 267–273.
[26] N. Nayan, G. Singh, S.V.S.N. Murty, A.K. Jha, B. Pant, K.M. George, U. Ramamurty, Intermetallics Hot deformation behaviour and microstructure control in AlCrCuNiFeCo high entropy alloy, Intermetallics 55 (2014) 145–153, http://dx.doi.org/10.1016/j.intermet.2014.07.019.
[27] N. Nayan, G. Singh, S.V.S. Narayana Murty, A.K. Jha, B. Pant, K.M. George, High-temperature deformation processing map approach for obtaining the desired microstructure in a multi-component (Ni-Ti-Cu-Fe) alloy, Metall. Mater. Trans. A 46 (2015) 2201–2215, http://dx.doi.org/10.1007/s11661-015-2799-2.
[28] A.A. Guimaraes, J.J. Jonas, Recrystallization and aging effects associated with the high temperature deformation of waspaloy and inconel 718, Metall. Trans. A 12 (1981) 1655–1666.
[29] S. Semiatin, V. Seetharaman, I. Weiss, Flow behavior and globularization kinetics during hot working of Ti–6Al–4 V with a colony alpha microstructure, Mater. Sci. Eng. A 263 (1999) 257–271, http://dx.doi.org/10.1016/S0921-5093(98)01156-3.
[30] S. Samal, K. Biswas, Novel high-strength NiCuCoTiTa alloy with plasticity, J. Nanopart. Res. 15 (2013) 1–11, http://dx.doi.org/10.1007/s11051-013-1783-2.
[31] Q.L. Dai, B.B. Sun, M.L. Sui, G. He, Y. Li, J. Eckert, et al., High-performance bulk Ti-Cu-Ni-Sn-Ta nanocomposites based on a dendrite-eutectic microstructure, J. Mater. Res. 19 (2011) 2557–2566, http://dx.doi.org/10.1557/JMR.2004.0332.
[32] Y. Zhang, J. Qiao, P.K. Liaw, A brief review of high entropy alloys and serration behavior and flow units, J. Iron Steel Res. Int. 23 (2016) 2–6, http://dx.doi.org/10.1016/S1006-706X(16)30002-4.
[33] J. Antonaglia, X. Xie, Z. Tang, C.W. Tsai, J.W. Qiao, Y. Zhang, M.O. Laktionova, E. D. Tabachnikova, J.W. Yeh, O.N. Senkov, M.C. Gao, J.T. Uhl, P.K. Liaw, K. A. Dahmen, Temperature effects on deformation and serration behavior of high-entropy alloys (HEAs), Jom 66 (2014) 2002–2008, http://dx.doi.org/10.1007/s11837-014-1130-9.
[34] T. Sakthivel, K. Laha, M. Nandagopal, K.S. Chandravathi, P. Parameswaran, S. P. Selvi, M.D. Mathew, S.K. Mannan, Effect of temperature and strain rate on serrated flow behaviour of Hastelloy X, Mater. Sci. Eng. A 534 (2012) 580–587, http://dx.doi.org/10.1016/j.msea.2011.12.011.
[35] S. Roy, S. Suwas, The influence of temperature and strain rate on the deformation response and microstructural evolution during hot compression of a titanium alloy Ti–6Al–4V–0.1B, J. Alloy. Compd. 548 (2013) 110–125, http://dx.doi.org/10.1016/j.jallcom.2012.08.123.
[36] Y.V.R.K. Prasad, H.L. Gegel, S.M. Doraivelu, J.C. Malas, J.T. Morgan, K.A. Lark, D. R. Barker, Modeling of dynamic material behavior in hot deformation: Forging of Ti-6242, Metall, Trans. A 15 (1984) 1883–1892, http://dx.doi.org/10.1007/BF02664902.
[37] Y.V.R.K. Prasad, K.P. Rao, Processing maps and rate controlling mechanisms of hot deformation of electrolytic tough pitch copper in the temperature range 300–950 °C, Mater. Sci. Eng. A 391 (2005) 141–150, http://dx.doi.org/10.1016/j.msea.2004.08.049.
[38] Y.V.R.K. Prasad, K.P. Rao, S. Sasidhara, Hot Working Guide: Compendium of Processing Maps, ASM International, Materials Park, OH, 2015.